AIAA JOURNAL
Vol. 39, No. 7, July 2001

Simulation of Vortex Breakdown Using Adaptive Grid Refinement with Vortex-Center Identification

Mitsuhiro Murayama,* Kazuhiro Nakahashi,† and Keisuke Sawada‡
Tohoku University, Sendai 980-8579-01, Japan

A topological-feature adaptation method is proposed to compute vortical flows around a delta wing at high incidence. Vortex-center identification based on the locally applied critical-point method is utilized as an indicator of the grid refinement using Rivara's bisection algorithm (Rivara, M. C., "Selective Refinement/Definement Algorithms for Sequences of Nested Triangulations," *International Journal of Numerical Methods in Engineering*, Vol. 28, 1989, pp. 2889–2906). The three-dimensional Navier–Stokes equations are solved using the hybrid unstructured grid. The computed results show that the refinement at the vortex core is effective to improve the numerical accuracy of the flow around a delta wing. The present feature-adaptive refinement is especially effective to improve the prediction of the vortex breakdown positions at high incidence. The results indicate the importance of the resolution at the vortex core for an accurate prediction of vortex-dominated flowfields.

Introduction

FLOWS around a delta wing at high incidence are largely governed by the leading-edge separation. This separation vortex may generate a large nonlinear lift increment, called vortex-induced lift at moderate angles of attack. At higher angles of attack, however, this vortex may burst, resulting in a sudden decrease of the lift. It is important to understand and predict such flowfields dominated by vortices for prediction and control of the vortex breakdown of a delta wing at high incidence, for the empennage buffeting by the vortex breakdown, and for the interaction between the helicopter blade and the tip vortex.

Recently, such complex flow problems have been numerically investigated by large-scale computations. To obtain accurate numerical results with the limited capacity of the computer, the grid points have to be allocated properly. However, local characteristic lengths of a flow depend highly on the flow condition and configuration. It is almost impossible to generate a grid according to local flow scales without knowing the resulting flowfield. The adaptive grid refinement method, therefore, is very useful for practical computations. Several effective methods have been proposed.[1–5]

For the use of adaptive grids, it is essential to choose the indicator for the grid refinement. For transonic and supersonic flows, gradient or second derivatives of the density have been successfully used for resolving shock waves and shear layers.[1] The methods that use the truncation error as the grid refinement indicator are also ideal. On the other hand, for the vortical flows, such as the leading-edge separation on a delta wing at high incidence and the wing tip vortex, it is difficult to select a proper criterion for adaptation. The conventional density gradient is not effective at low subsonic flows. Gradients or second derivatives of the total pressure or the vorticity may be better indicators. However, these indicators are often very noisy.

Moreover, a threshold for the indicator has to be determined for the field variables to control the degree of adaptation. A larger value of the threshold of the indicator cannot improve the computational accuracy, whereas a smaller value may result in too great a concentration of grid points, causing the failure to utilize the given computational environment. A proper threshold can be found only on a trial-and-error basis.

In this paper, topological features of flows are utilized as an indicator of the adaptive grid refinement instead of the conventional field indicators. When a vortical flow around a delta wing at high incidence is considered, the vortex centerlines characterize the flowfield and are often used for the flow visualization. One of the advantages of the topological features instead of the gradient of flow variables as the adaptation indicator is that the important regions for flowfields are identified easily and refined effectively. Once the characteristic topology is identified in the flowfield, grid refinement can be applied to the grid cells marked by the topological feature.

The objective of this paper is to examine the effectiveness of the topological adaptation instead of the gradient adaptation for vortical flows over a delta wing. A vortex-center identification method proposed by Sawada[6] is coupled with the unstructured grid refinement method. The relationship between the grid resolution around the vortex center and the vortex breakdown predictions is also examined. The vortex breakdown is considered to have a strong relationship with the streamwise pressure gradient along the longitudinal vortex core. Therefore, the adaptive refinement at the vortex core can be expected to improve the accuracy of the vortex breakdown predictions.

Vortex-Center Identification Method

There are several methods to identify vortex centers.[7–12] One approach is to take the relevant physical quantity such as the vorticity and the helicity density. The helicity density is a dot product of velocity and vorticity. Because those two vectors point at the same direction at the vortex core, the vortex centerline can be easily found.

Another approach is to use critical-point analysis.[7–9] In this approach, the velocity field is expanded around the critical point, where the velocity becomes zero and the slope of the streamline becomes indeterminate. The local structure of the flowfield is related to the characteristics of the coefficient matrix that appears as the leading term in the series expansion of the velocity field. The vortex centerline at the critical point is parallel to the eigenvector of the real eigenvalue of the coefficient matrix. Thus, the vortex centerline near the critical point can be identified by finding the critical point and the associated eigenvector. A higher-order streamline integration is employed to obtain the extended vortex centerline apart from the critical point. In general, however, it is difficult to follow the vortex centers apart from the critical point especially when the vortex center exhibits a significant wavy pattern. In the case of the longitudinal vortex, which has an apparent axis, it is possible to identify the critical point by the projection of the velocity fields on the vertical section of the vortex axis. However, application of the projection is difficult when the axis direction changes and it cannot be forecast.

In this study, a vortex-center identification method proposed by Sawada[6] is employed. It applies the critical-point analysis locally. In this method, streamlines are semi-analytically constructed using the assumption that the local velocity field can be linearly parameterized in a tetrahedral computational cell as shown in Fig. 1:

Received 3 June 2000; revision received 7 November 2000; accepted for publication 18 January 2001.

*Graduate Student, Department of Aeronautics and Space Engineering.
†Professor, Department of Aeronautics and Space Engineering. Associate Fellow AIAA.
‡Professor, Department of Aeronautics and Space Engineering. Senior Member AIAA.

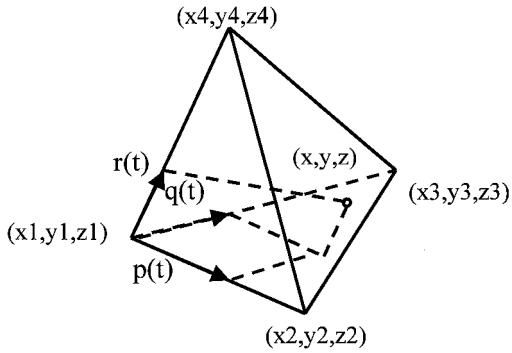

Fig. 1 Parameter space in a tetrahedral computational cell.

$$\begin{pmatrix} x \\ y \\ z \end{pmatrix} = \begin{pmatrix} x_1 \\ y_1 \\ z_1 \end{pmatrix} + \begin{pmatrix} x_2 - x_1 & x_3 - x_1 & x_4 - x_1 \\ y_2 - y_1 & y_3 - y_1 & y_4 - y_1 \\ z_2 - z_1 & z_3 - z_1 & z_4 - z_1 \end{pmatrix} \begin{pmatrix} p \\ q \\ r \end{pmatrix} \tag{1}$$

$$\begin{pmatrix} u \\ v \\ w \end{pmatrix} = \begin{pmatrix} u_1 \\ v_1 \\ w_1 \end{pmatrix} + \begin{pmatrix} u_2 - u_1 & u_3 - u_1 & u_4 - u_1 \\ v_2 - v_1 & v_3 - v_1 & v_4 - v_1 \\ w_2 - w_1 & w_3 - w_1 & w_4 - w_1 \end{pmatrix} \begin{pmatrix} p \\ q \\ r \end{pmatrix} \tag{2}$$

where (u_i, v_i, w_i) are the velocity components at the corresponding vertices. The parameters (p, q, r), which are assumed to be the functions of time t, should satisfy the following conditions:

$$0 \le p, q, r, \qquad p + q + r \le 1 \tag{3}$$

The streamline equations in the three-dimensional field can be written as

$$\frac{\mathrm{d}x}{u} = \frac{\mathrm{d}y}{v} = \frac{\mathrm{d}z}{w} = \mathrm{d}t \tag{4}$$

For the local linear assumption, these streamline equations can be written as

$$\begin{pmatrix} \dfrac{\mathrm{d}p}{\mathrm{d}t} \\ \dfrac{\mathrm{d}q}{\mathrm{d}t} \\ \dfrac{\mathrm{d}r}{\mathrm{d}t} \end{pmatrix} = \begin{pmatrix} a_{11} & a_{12} & a_{13} \\ a_{21} & a_{22} & a_{23} \\ a_{31} & a_{32} & a_{33} \end{pmatrix} \begin{pmatrix} p \\ q \\ r \end{pmatrix} + \begin{pmatrix} \boldsymbol{b}_1 \\ \boldsymbol{b}_2 \\ \boldsymbol{b}_3 \end{pmatrix} \tag{5}$$

where a_{ij} and $\boldsymbol{b}_i$ are the coefficient matrix and the coefficient vector that are given analytically from the coordinates and velocity components at the vertices of the tetrahedral cell.

These equations can be rearranged as a set of third-order, constant-coefficient, linear differential equations. For the parameter p, the equation is

$$\frac{\mathrm{d}^3 p}{\mathrm{d}t^3} - \alpha \frac{\mathrm{d}^2 p}{\mathrm{d}t^2} + \beta \frac{\mathrm{d}p}{\mathrm{d}t} - \gamma p = k_p \tag{6}$$

where coefficients α, β, γ, and k_p are constants composed of a_{ij} and $\boldsymbol{b}_i$. Solution of Eq. (6) depends on the characteristics of the coefficient matrix. For example, if the characteristic equation has three distinct roots λ_i, $p(t)$ will take the following form:

$$p(t) = \boldsymbol{A}_1 e^{\lambda_1 t} + \boldsymbol{A}_2 e^{\lambda_2 t} + \boldsymbol{A}_3 e^{\lambda_3 t} - (k_p/\gamma) \tag{7}$$

where coefficients $\boldsymbol{A}_i$ are constants and can be determined by the initial conditions.

If the characteristic equation has one real root λ_1 and two conjugate complex roots λ_2 and λ_3, then the local streamline within the cell draws a spiral pattern. Analytic solution for the local velocity field can be given, and the following analytic equations for the vortex center can be obtained from Eq. (7):

$$\frac{p + (k_p/\gamma)}{\boldsymbol{A}_1} = \frac{q + (k_q/\gamma)}{\boldsymbol{B}_1} = \frac{r + (k_r/\gamma)}{\boldsymbol{C}_1} \tag{8}$$

Equation (8) represents a straight line through the point $(-k_p/\gamma, -k_q/\gamma, -k_r/\gamma)$ in the parameter space whose direction is parallel to the vector $(\boldsymbol{A}_1, \boldsymbol{B}_1, \boldsymbol{C}_1)$. Here, it can be shown that the vector $(\boldsymbol{A}_1, \boldsymbol{B}_1, \boldsymbol{C}_1)^T$ is the right eigenvector of the coefficient matrix a_{ij} in Eq. (5) with the associated real eigenvalue λ_1. Thus, Eq. (8), the possible vortex centerline, is identified as a unique straight line in the parameter space. In case the straight line crosses the computational tetrahedral cell, the line segment inside the tetrahedral cell is taken as the local vortex centerline. The line segments of the vortex centerline are defined in this way, and as a result, a collection of these line segments represents the overall vortex centerline.

Although this method is similar to the critical point analysis, it has several unique advantages. In this method, there is no need for projection or the high-order streamline integration because the vortex centerline is defined locally one by one. This feature is favorable for unstructured grids, which consist of tetrahedral computational cells. Although the present method may produce discontinuous vortex centerline in a coarse grid, it will be good enough for indicating the area of grid refinement.

Adaptive Refinement Method

To compute the boundary layer accurately and efficiently, the hybrid unstructured grid method is used. The hybrid grids comprising tetrahedra, prisms, and pyramids are generated by the method described in Ref. 13. The prismatic semistructured grid is generated around viscous boundary surfaces and covers viscous regions whereas the tetrahedral grid covers the rest of the computational domain. Pyramid grids are used for the junction at prismatic and tetrahedral grids. The Delaunay approach for tetrahedral grid generation is used. The proposed prismatic grid is structured in directions normal to the boundary faces, but the number of prisms generated from each boundary face is variable from face to face for the flexibility of the grid generation.

An adaptive grid refinement method is used to increase the mesh resolution in the vicinity of the vortex centers. Variations of the flow variables, such as the density and total pressure, were used as an indicator of the grid refinement.[14] However, such an indicator is sometimes very noisy, as shown in Fig. 2. Moreover, the degree of the refinement depends on the threshold of the indicator. The threshold has to be found by trial and error.

Here, we use the distinct topological flow feature, vortex centerlines, identified by the vortex-center identification method as the refinement indicator. When the topological feature is used, the present method can refine the most important regions effectively and decrease a time-consuming task for grid refinement. It is also interesting to see the relationship between the resolution of a vortex core and the breakdown prediction. Here, the cells containing the vortex centerlines and its neighboring cells are flagged for the refinement.

The refinement algorithm employed in this study is Rivara's bisection algorithm[15] (also see Ref. 2). A tetrahedron is bisected by a plane passing through the midpoint of its longest edge and through the nodes opposite to this edge. If an edge of the tetrahedron has already been bisected, the element is marked for refinement. The process is repeated until no marked tetrahedra remain.

This method is extended to the hybrid grid used here in the following order:

1) The cells containing the vortex centerlines and its neighboring cells are flagged.

2) The tetrahedrons are divided using the bisection algorithm.

3) The pyramids connecting to the divided tetrahedrons are divided.

4) The prisms connecting to the divided pyramids and tetrahedrons are divided.

5) The prisms below the divided prisms are divided one after another until the division reaches the boundary surface.

Flow Solver

The three-dimensional Navier–Stokes equations can be expressed in an integral form as follows:

$$\frac{\partial}{\partial t} \int_{\Omega} \boldsymbol{Q}\, \mathrm{d}V + \int_{\partial\Omega} [\boldsymbol{F}(\boldsymbol{Q}) - \boldsymbol{G}(\boldsymbol{Q})] \cdot \boldsymbol{n}\, \mathrm{d}S = 0 \tag{9}$$

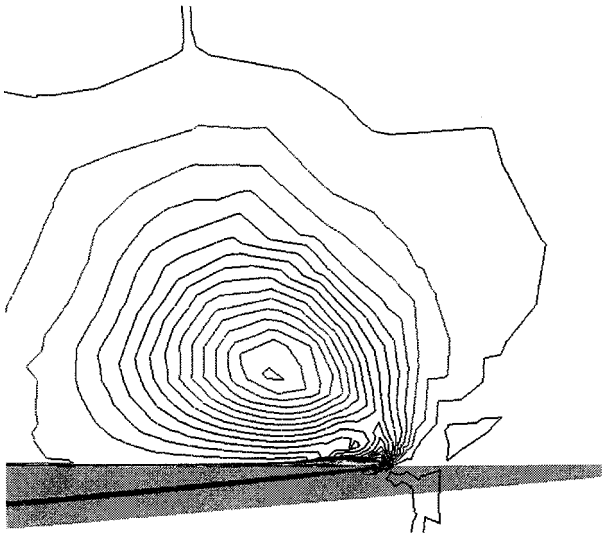

Total pressure contours

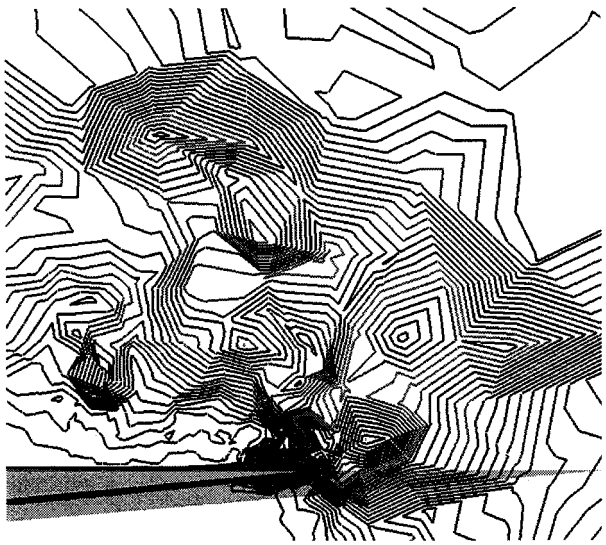

Second derivatives of the total pressure

Fig. 2 Conventional index for adaptation on a delta wing.

where $\boldsymbol{Q} = [\rho, \rho u, \rho v, \rho w, e]^T$ is the vector of conservative variables; ρ is the density; u, v, and w are the velocity components in the x, y, and z directions; and e is the total energy. The vectors $\boldsymbol{F}(\boldsymbol{Q})$ and $\boldsymbol{G}(\boldsymbol{Q})$ represent the inviscid and viscous flux vectors, and $\boldsymbol{n}$ is the outward normal of $\partial\Omega$, which is the boundary of the control volume Ω. This system of equations is closed by the perfect gas equation of state.

The equations are solved by a finite volume cell-vertex scheme, where the control volume Ω_i at mesh i is a nonoverlapped dual cell. With this control volume boundary, Eq. (9) can be written in an algebraic form as follows:

$$\frac{\partial \boldsymbol{Q}_i}{\partial t} = -\frac{1}{V_i}\left[\sum_{j(i)} \Delta S_{ij} \boldsymbol{h}\left(\boldsymbol{Q}_{ij}^{+}, \boldsymbol{Q}_{ij}^{-}, \boldsymbol{n}_{ij}\right) - \sum_{j(i)} \Delta S_{ij} \boldsymbol{G}(\boldsymbol{Q}_{ij}, \boldsymbol{n}_{ij})\right] \tag{10}$$

where ΔS_{ij} is a segment area of the control volume boundary associated with the edge connecting points i and j. The term $\boldsymbol{h}$ is an inviscid numerical flux vector normal to the control volume boundary, and $\boldsymbol{Q}_{ij}^{\pm}$ are values on both sides of the control volume boundary. The subscript of summation, $j(i)$, refers to all node points connected to node i.

The Harten–Lax–van Leer–Einfeldt–Wada Riemann solver (see Ref. 16) is used for the numerical flux computations. Second-order spatial accuracy is realized by a liner reconstruction of the primitive variables $\boldsymbol{q} = [\rho, u, v, w, p]^T$ inside the control volume, namely,

$$\boldsymbol{q}(x, y, z) = \boldsymbol{q}_i + \Psi_i \nabla \boldsymbol{q}_i \cdot (\boldsymbol{r} - \boldsymbol{r}_i) \tag{11}$$

where $\boldsymbol{r}$ is a vector pointing to point (x, y, z) and i is the node number. The gradients associated with the control volume centroids are volume-averaged gradients computed using the value in the surrounding grid cells. A limiter Ψ is used to make the scheme monotone. Here Venkatakrishnan's limiter[17] is used because of its superior convergence properties.

To compute viscous stress and the heat flux terms in $\boldsymbol{G}(\boldsymbol{Q})$, spatial derivatives of the primitive variables at each control volume face are evaluated directly at the edges.

The lower–upper-symmetric Gauss–Seidel (LU-SGS) implicit method, originally developed for structured grids (see Ref. 18) is applied to compute the high-Reynolds-number flows efficiently. The LU-SGS method on an unstructured grid can be derived by splitting node points $j(i)$ into two groups, $j \in L(i)$ and $j \in U(i)$, for the first summation in the left-hand side of Eq. (10). With $\Delta\boldsymbol{Q} = \Delta\boldsymbol{Q}^{n+1} - \Delta\boldsymbol{Q}^{n}$, the final form of the LU-SGS method for the unstructured grid becomes the following two sweeps.

Forward sweep:

$$\Delta\boldsymbol{Q}^{*} = \boldsymbol{D}^{-1}\left[\boldsymbol{R}_i - 0.5 \sum_{j \in L(i)} \Delta S_{ij}\left(\Delta\boldsymbol{h}_j^{*} - \rho_A \Delta\boldsymbol{Q}_j^{*}\right)\right] \tag{12a}$$

Backward sweep:

$$\Delta\boldsymbol{Q}_i = \Delta\boldsymbol{Q}_i^{*} - 0.5\boldsymbol{D}^{-1} \sum_{j \in U(i)} \Delta S_{ij}(\Delta\boldsymbol{h}_j - \rho_A \Delta\boldsymbol{Q}_j) \tag{12b}$$

where $\Delta\boldsymbol{h} = \boldsymbol{h}(\boldsymbol{Q} + \Delta\boldsymbol{Q}) - \boldsymbol{h}(\boldsymbol{Q})$ and

$$\boldsymbol{D} = \left(\frac{V_j}{\Delta t} + 0.5 \sum_{j(i)} \Delta S_{ij} \rho_A\right)\boldsymbol{I}$$

$$\boldsymbol{R}_i = -\sum_{j(i)} \Delta S_{ij} \boldsymbol{h}_{ij}^{*} + \sum_{j(i)} \Delta S_{ij} \boldsymbol{G}_{ij}^{n}$$

$\boldsymbol{D}$ is diagonalized by the Jameson–Turkel approximation[19] of the Jacobian as $\boldsymbol{A}^{\pm} = 0.5(\boldsymbol{A} \pm \rho_A \boldsymbol{I})$, where ρ_A is a spectral radius of Jacobian $\boldsymbol{A}$.

The lower–upper splitting of Eq. (12) for the unstructured grid is done by a grid reordering technique[20] that was developed to improve the convergence and the vectorization. For unsteady flow, the time accuracy of the LU-SGS solution algorithm is recovered by Newton iteration using the Crank–Nicolson method.

Results

Computational Model and Flow Condition

The geometry used in the present study is a slender delta wing of aspect ratio of unity and a sweep angle of 76 deg corresponding to the experiment by Hummel.[21] The axial direction coincides with the wing chord direction, and the apex sets $x = 0$ and the trailing edge $x = 1$. The outer boundary is a semisphere whose radius is a 10 root chord length. The first point above the wing surface is located at a distance of 10^{-4} root chord lengths. For the grid resolution around the leading edge, the surface grid is concentrated on the leading edge, as shown in Fig. 3. The total number of initial grid points is 302,810. The numbers of prismatic, tetrahedral, and pyramidal cells are 409,645, 510,289, and 63, respectively.

Solutions were obtained at a freestream Mach number $M_\infty = 0.3$ and several angles of attack for flows without vortex breakdown and with breakdown. The Reynolds number based on the root chord is 0.95×10^6 at angle of attack of 20.5 deg and 1.0×10^6 at the other angles of attack. Laminar flow was assumed because the experimental observation of Hummel[21] showed a laminar flow at most regions of the upper side of the wing.

Flows Without Vortex Breakdown

First, the solution at angle of attack of 20.5 deg, which did not have the vortex breakdown, was computed to examine the numerical accuracy of the present method. The computational results were compared with the available experimental measurements of Hummel[21] and Kjelgaard and Sellers.[22]

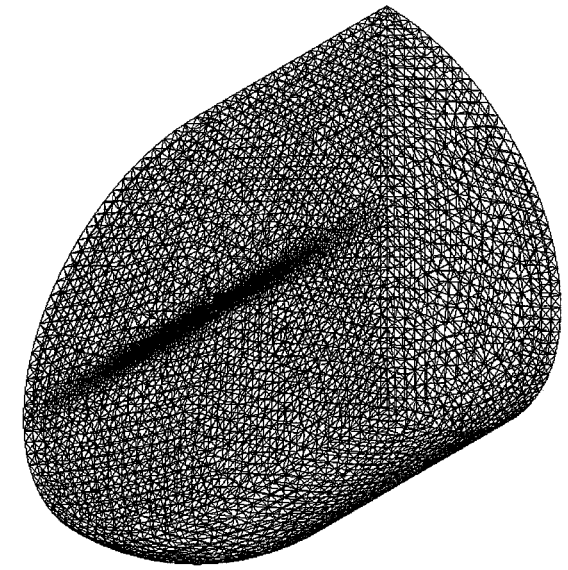

Outer boundary

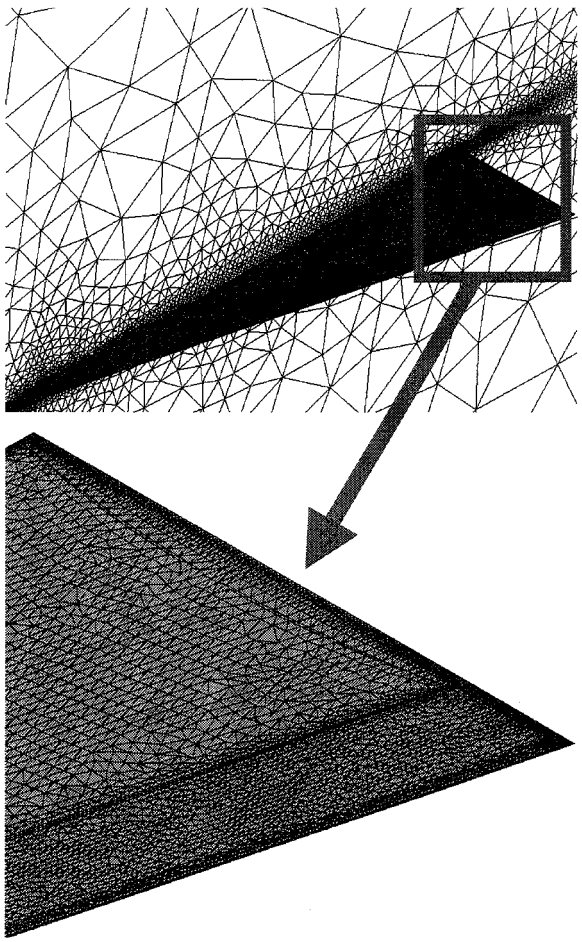

Closeup view of the wing surface

Fig. 3 Initial grid of the delta wing.

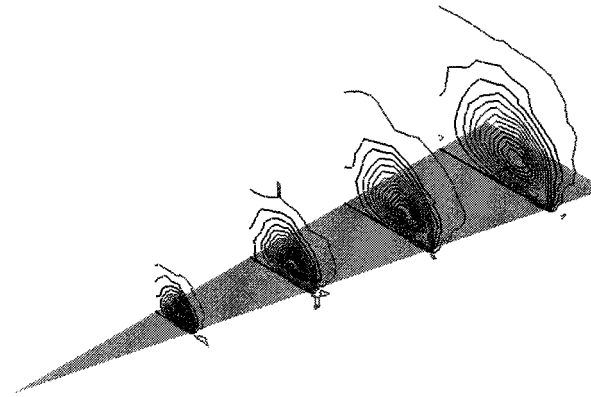

a) Total pressure contours on the streamwise cutting planes

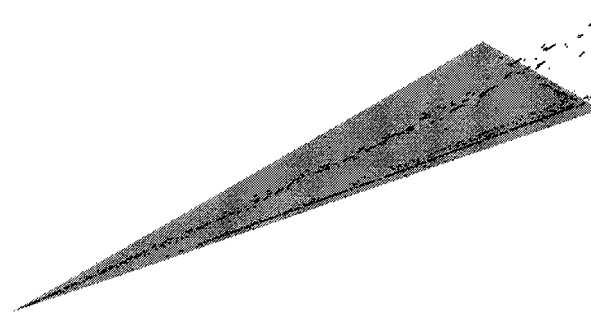

b) Identified vortex centerlines

Fig. 4 Total pressure contours and vortex centerlines by the initial grid: $\alpha = 20.5$ deg, $M = 0.3$, and $Re = 0.95 \times 10^6$.

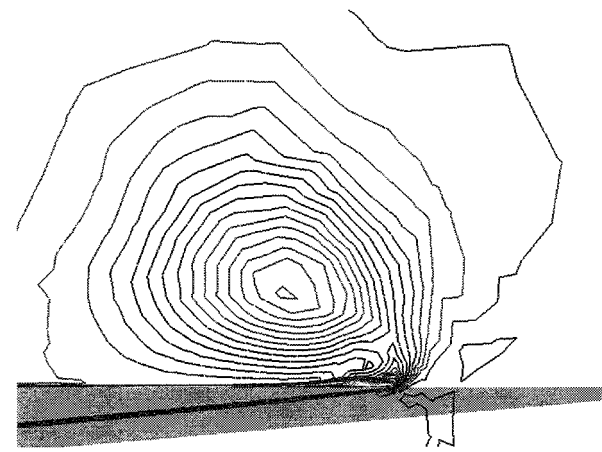

Fig. 5 Total pressure contours in the crossflow plane at $x = 0.5$ of the initial grid: $\alpha = 20.5$ deg, $M = 0.3$, and $Re = 0.95 \times 10^6$.

Figures 4a and 4b show the total pressure contours on several streamwise cutting planes and the identified vortex centerlines obtained on the initial grid. The total pressure contours on a cut view at $x = 0.5$ are shown in Fig. 5. In Figs. 4 and 5, a primary vortex due to the leading-edge separation can be observed. The secondary vortex induced by the adverse spanwise pressure gradients outboard of the primary vortex can also be seen, although it is not very clear. The primary and secondary vortex centerlines are identified by the collection of the line segments identified at each computational cell, although they are slightly discontinuous. The discontinuity of the vortex centerlines may be due to the insufficient grid resolution.

Grid refinement was applied to this initial grid using the identified vortex centers as the refinement indicator. The vortex-center identification method identifies the cells containing the vortex centerlines. These cells are flagged at first. Then, the extent of the grid refinement is controlled by specifying the depth of the neighboring cell search. In the following results, one-depth search, which identifies the neighboring cells to the vortex core cells, is performed for refinement, as shown in Fig. 6a.

Figures 6b and 6c show a cut view of the initial grid and the refined grid where the adaptive refinement was applied twice during the flow computation. The total number of the grid points refined once and the final grid points refined twice became 415,170 and 525,380, respectively. The total pressure contours and the corresponding vortex centerlines obtained on the adapted grid refined twice are shown in Figs. 7 and 8. When compared with the initial results in Figs. 4 and 5, the total pressure contours became smoother and the secondary vortices appeared more clearly. The more continuous

a) Cells containing the vortex centerlines and its neighboring cells for the refinement

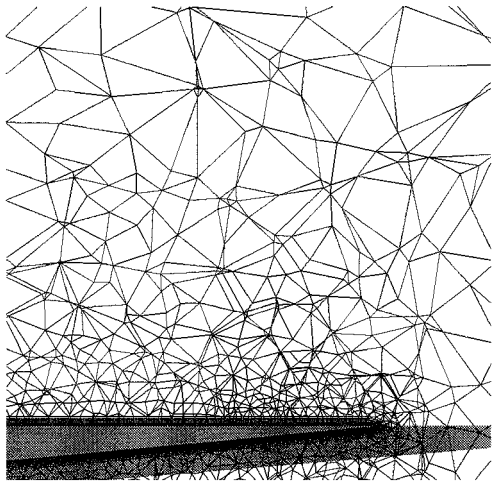

b) Cut view of the initial grid; $x = 0.5$

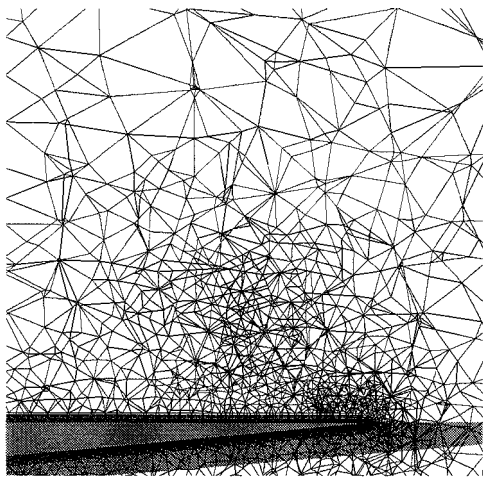

c) Cut view of the adapted grid; $x = 0.5$

Fig. 6 Adaptive refinement at $\alpha = 20.5$ deg.

vortex centerlines were obtained at the adapted grid, and the vortex centerlines of the secondary vortex were also recognized clearly. These vortex centerlines are very useful to understand the flow structure.

For the validation, the surface pressure coefficients at different axial locations were compared with experimental data[21] and results using second derivatives of the total pressure as the refinement index in Fig. 9. In the case of the total pressure adaptation, a threshold for the refinement was subjectively determined by trial and error, and the total number of the grid points became 529,728. In the case of the vortex-center adaptation, even one refinement, with fewer than 415,170 grid points, can improve the overall prediction of the pressure coefficients significantly. Thus, the present method can improve grid resolution effectively for the vortical flowfields.

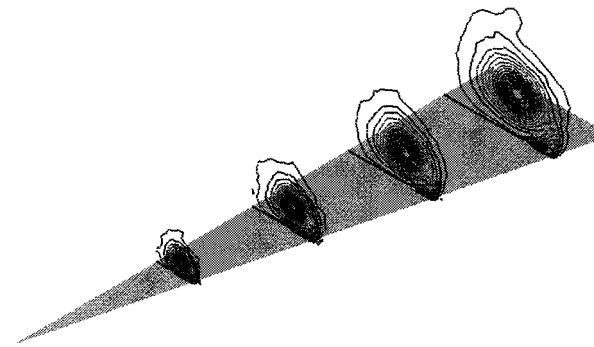

Total pressure contours on selected streamwise cutting planes

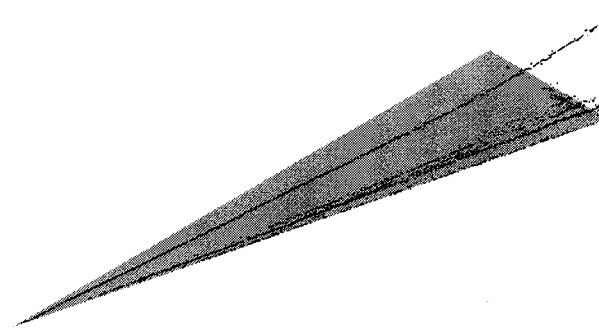

Identified vortex centerlines

Fig. 7 Total pressure contours and vortex centerlines by the adapted grid: $\alpha = 20.5$ deg, $M = 0.3$, and $Re = 0.95 \times 10^6$.

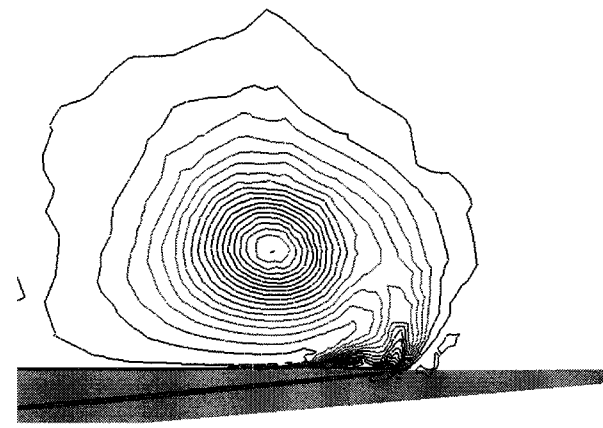

Fig. 8 Total pressure contours in the crossflow plane at $x = 0.5$ of the adapted grid: $\alpha = 20.5$ deg, $M = 0.3$, and $Re = 0.95 \times 10^6$.

Flows with Vortex Breakdown

At higher angle of attack, vortex breakdown will occur. This breakdown phenomenon has a strong relationship with the streamwise pressure gradient along the longitudinal vortex core, so that the grid refinement at the vortex core can be expected to improve the prediction accuracy of the breakdown position. In this section, the effectiveness of the present method to predict the vortex breakdown for the flows at higher angles of attack is discussed.

When the angle of attack was increased, a vortex breakdown appeared first at $\alpha = 32$ deg in the computation. This breakdown was predicted only with the adaptive grid after two cycles of adaptation and not with the initial grid. The crossflow views at $x = 0.9$ and streamlines from the wing apex are shown for the initial grid and adapted grid in Figs. 10 and 11, respectively. In Fig. 11b, the streamlines starting from the wing apex show the vortex breakdown pattern near the trailing edge of the delta wing.

To discuss the effectiveness of the present method, the adaptive method using second derivatives of the total pressure as the refinement index is compared with the present method. The predicted vortex breakdown positions by the number of the refinement cycles

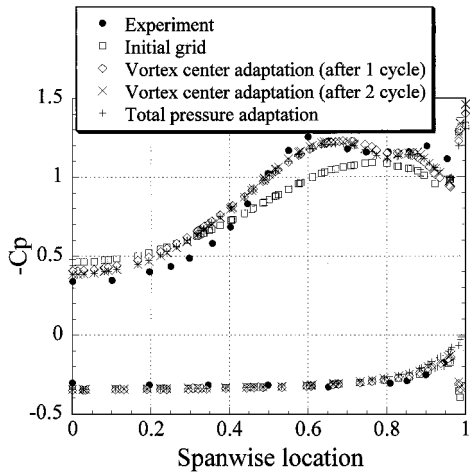

Surface pressure coefficients; $x = 0.3$

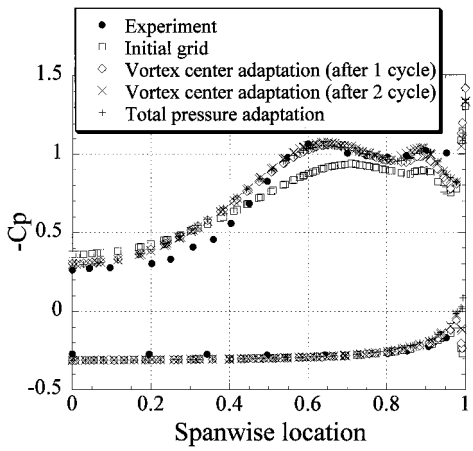

Surface pressure coefficients; $x = 0.5$

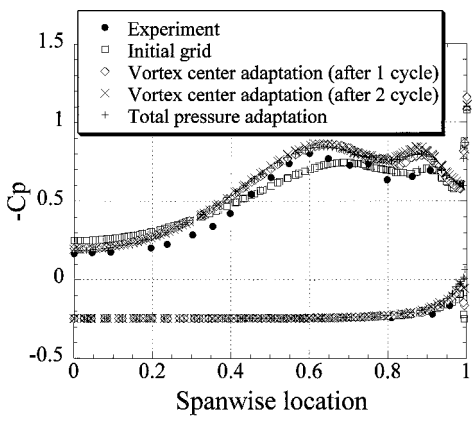

Surface pressure coefficients; $x = 0.7$

Fig. 9 Surface pressure coefficients at different axial locations: $\alpha = 20.5$ deg, $M = 0.3$, and $Re = 0.95 \times 10^6$.

are shown in Table 1. The number of grid points after the adaptations are shown in Fig. 12.

The crossflow view at $x = 0.9$ and streamlines from the wing apex obtained by the grid using the second derivatives of the total pressure are shown in Fig. 13. The overall grid density around the vortex in the total pressure adaptation became larger than the vortex-center adaptation, but the vortex breakdown did not appear at all. The total pressure adaptation required three cycles of adaptation to predict the vortex breakdown at $\alpha = 32$ deg. The total number of the node points with this adaptation became two times larger than the case of the vortex-centerline adaptation. At $\alpha = 40$ deg, the tendency is the same as for the case at $\alpha = 32$ deg, although vortex breakdown was resolved reasonably after two cycles of adaptation.

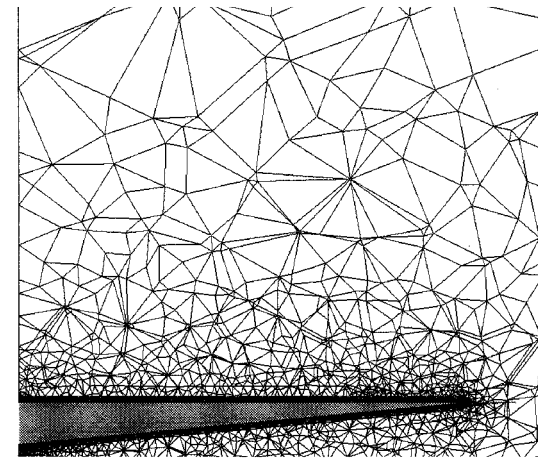

Crossflow view at $x = 0.9$

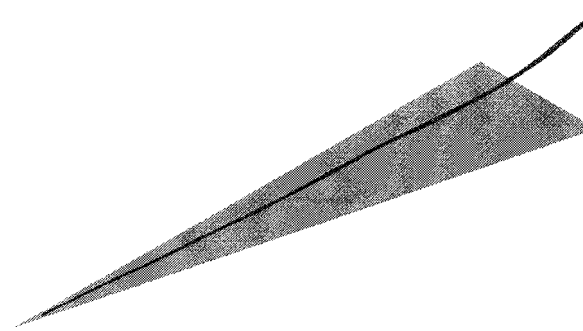

Streamline

Fig. 10 Computed results by the initial grid: $M = 0.3$, $Re = 1.0 \times 10^6$, and $\alpha = 32$ deg.

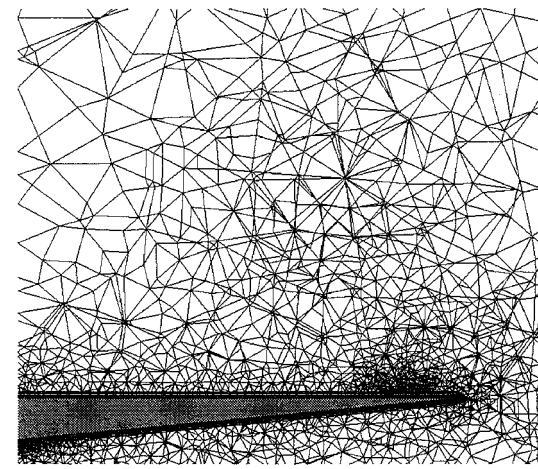

a) Crossflow view at $x = 0.9$

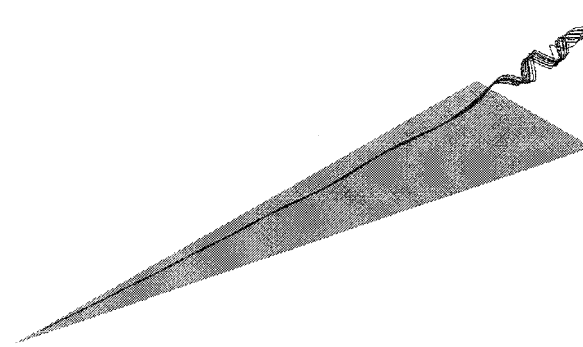

b) Streamline

Fig. 11 Computed results by the grid adapted to vortex centerlines (two-cycle adaptation): $M = 0.3$, $Re = 1.0 \times 10^6$, and $\alpha = 32$ deg.

Table 1 Vortex breakdown position using different indicators

Refinement cycle	Breakdown position: Vortex-center adaptation	Breakdown position: Total pressure adaptation
x/c ≒0.77 Hummel experiment, α = 32 deg		
1	——	——
2	0.9023	——
3	0.85	0.8842
x/c ≒0.4 Hummel experiment, α = 40 deg		
1	0.6912	——
2	0.38	0.4446
3	0.428	0.498

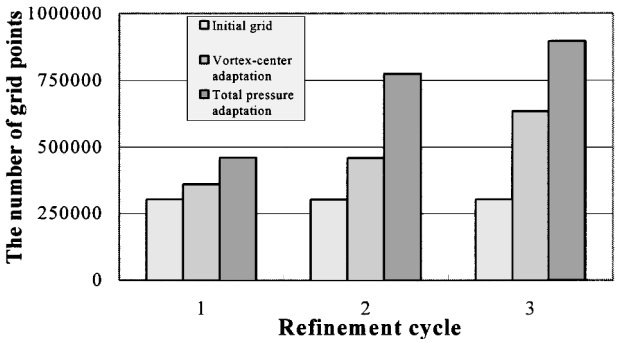

Fig. 12 Increment of grid points by the grid refinement.

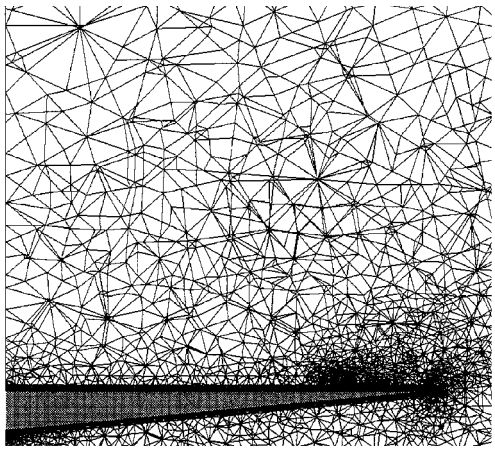

Crossflow view at $x = 0.9$

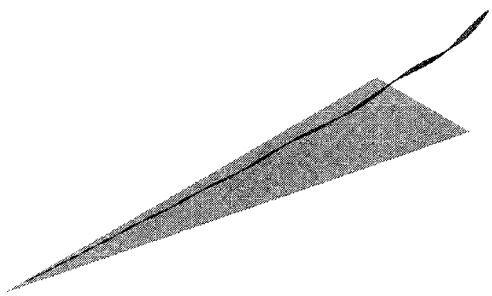

Streamline

Fig. 13 Computed results by the grid adapted to the second derivatives of the total pressure: $M = 0.3$, $Re = 1.0 \times 10^6$, and $\alpha = 32$ deg.

From these results, it can be said that better results can be obtained by the present feature-adaptation method at lower computational costs: fewer number of refinement cycles and fewer grid points. It also can be said that the grid resolution around the vortex core is very important for the accurate prediction of the vortex breakdown, as discussed in Ref. 23. In the conventional field-value adaptation, the threshold for refinement must be determined carefully. The number of grid points in the conventional field-value adaptation may become

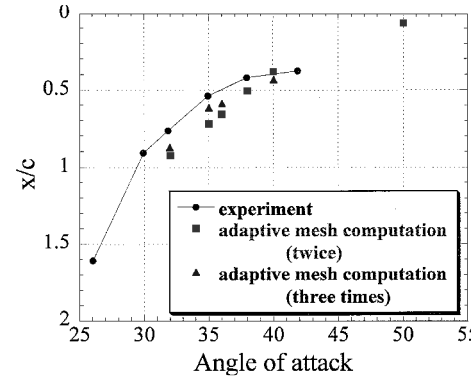

Fig. 14 Variation of vortex breakdown positions.

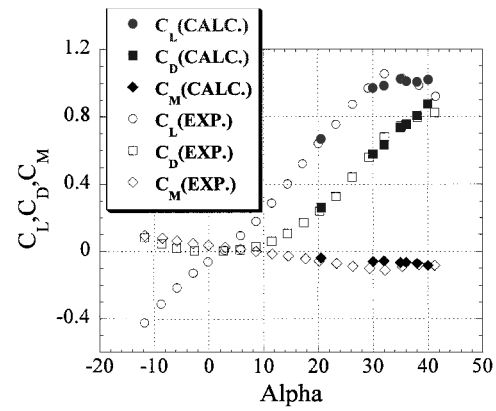

Fig. 15 Lift, drag, and pitching moment coefficients C_L, C_D, and C_M vs angle of attack.

lower if we select more a proper value of the threshold carefully and retry grid refinement because we decide the threshold for refinement intuitively and subjectively. However, it will require a lot of work because of the intuitive procedure. Thus, it will be clear that the present method is more effective.

The vortex breakdown positions with the variation of angles of attack are compared with the experiment of Hummel and Srinivasan[24] in Fig. 14. Computational results with the adaptive mesh show good agreement with the experiment, although the computed breakdown positions tend to be behind the experimental results. This small discrepancy between the computational and the experimental results may come from the different definition of the breakdown position. In the present computations, the vortex breakdown position is defined as the location where the velocity component in the x direction first becomes negative. In the experiment, the vortex breakdown is defined as the rapid expansion of the core of the vortex visualized by smoke or dye. This rapid expansion of the core occurs forward of the stagnation position.

Vortex breakdown was resolved reasonably well after only two cycles of adaptation at any angle of attack. In the bisection algorithm, a cell is divided at most into two cells per cycle. Therefore, several cycles of the refinement are required. The two cycles of adaptation seems to be good enough for the present cases, although the computational results with three cycles of adaptation show a slightly better agreement with experiments. The number of the grid points became about 1.5 times greater for two cycles of adaptation and almost twice as much for three cycles of adaptation.

Figure 15 shows the computed lift, drag, and pitching moment coefficients C_L, C_D, and C_M as a function of angle of attack by two refinements. They are compared with experimental results.[21] The computed results show good agreement with the experiment for the case without vortex breakdown. However, the numerical results for the lift reduction by the vortex breakdown are not as good, which may be due to the transition to turbulent flow by the vortex breakdown. Further investigation of a suitable turbulence model may be required.

Conclusions

An effective adaptive refinement method using vortex centerlines, which is a topological feature of flows, as a refinement indicator has been developed to compute the vortical flows around a delta wing at high incidence. The feature-adaptation method has an advantage that it can refine the most important regions effectively and decrease a time-consuming task to select the threshold value that is required in the conventional adaptive index. The present feature adaptation improves the prediction of the vortex breakdown locations effectively compared with the conventional adaptive grid method using the variations of flow variables.

References

[1]Nakahashi, K., and Deiwert, G. S., "Three-Dimensional Adaptive Grid Method," *AIAA Journal*, Vol. 24, No. 6, 1986, pp. 948–045.

[2]Sharov, D., and Fujii, K., "Three-Dimensional Adaptive Bisection of Unstructured Grids for Transient Compressible Flow Computations," AIAA Paper 95-1708, 1995.

[3]Löhner, R., "Adaptive H-Refinement on Three-Dimensional Unstructured Grids for Transient Problems," AIAA Paper 89-0365, 1989.

[4]Connel, S. D., and Holmes, D. G., "Three-Dimensional Unstructured Adaptive Multigrid Scheme for the Euler Equations," *AIAA Journal*, Vol. 32, No. 8, 1994, pp. 1626–1632.

[5]Kallinderis, Y., and Vijayan, P., "Adaptive Refinement-Coarsening Scheme for Three-Dimensional Unstructured Meshes," *AIAA Journal*, Vol. 31, No. 8, 1993, pp. 1440–1447.

[6]Sawada, K., "A Convenient Visualization Method for Identifying Vortex Centers," *Transactions of the Japan Society for Aeronautical and Space Sciences*, Vol. 38, No. 120, 1995, pp. 102–116.

[7]Perry, A. E., and Chong, M. S., "A Description of Eddying Motions and Flow Patterns Using Critical-Point Concepts," *Annual Review of Fluid Mechanics*, Vol. 19, 1987, pp. 125–155.

[8]Hesselink, L., and Helman, J., "Evaluation of Flow Topology from Numerical Data," AIAA Paper, 87-1181, 1987.

[9]Shirayama, S., "Flow Past a Sphere: Topological Transitions of the Vorticity Field," *AIAA Journal*, Vol. 30, No. 2, 1992, pp. 349–358.

[10]Jeong, J., and Hussain, F., "On the Identification of a Vortex," *Journal of Fluid Mechanics*, Vol. 285, 1995, pp. 69–94.

[11]Chong, M. S., and Perry, A. E., "A General Classification of Three-Dimensional Flow Fields," *Physics of Fluids A*, Vol. 2, No. 5 1990, pp. 765–777.

[12]Haimes, R., and Kenwright, D., "On the Velocity Gradient Tensor and Fluid Feature Extraction," AIAA Paper 99-3288, 1999.

[13]Sharov, D., and Nakahashi, K., "Hybrid Prismatic/Tetrahedral Grid Generation for Viscous Flow Applications," *AIAA Journal*, Vol. 36, No. 2, 1998, pp. 157–162.

[14]Kano, S., and Nakahashi, K., "Navier–Stokes Computations of HSCT Off-Design Aerodynamics Using Unstructured Hybrid Grids," AIAA Paper 98-0232,1998.

[15]Rivara, M. C., "Selective Refinement/Derefinement Algorithms for Sequences of Nested Triangulations," *International Journal of Numerical Methods in Engineering*, Vol. 28, 1989, pp. 2889–2906.

[16]Obayashi, S., and Guruswamy, G. P., "Convergence Acceleration of an Aeroelastic Navier–Stokes Solver," AIAA Paper 94-2268, 1994.

[17]Venkatakrishnan, V., "On the Accuracy of Limiters and Convergence to Steady-State Solutions," AIAA Paper 93-0880, 1993.

[18]Jameson, A., and Yoon, S., "Lower–Upper Implicit Schemes with Multiple Grids for the Euler Equations," *AIAA Journal*, Vol. 25, No. 7, 1987, pp. 929–935.

[19]Jameson, A., and Turkel, E., "Implicit Schemes and LU Decompositions," *Mathematics of Computation*, Vol. 37, No. 156, 1981, pp. 385–397.

[20]Sharov, D., and Nakahashi, K., "Reordering of Three-Dimensional Hybrid Unstructured Grids for Vectorized LU-SGS Navier–Stokes Computations," AIAA Paper 97-2102, 1997.

[21]Hummel, D., "On the Vortex Formation over a Slender Wing at Large Angle of Incidence," *High Angle of Attack Aerodynamics*, CP-247, AGARD, 1979, pp. 15-1–15-17.

[22]Kjelgaard, S. O., and Sellers, W. L., III, "Detailed Flowfield Measurement over a 75-Degree Swept Delta Wing for Code Validation," *Validation of Computational Fluid Dynamics*, Vol. 2, CP-437, AGARD, 1988, pp. 10-1–10-14.

[23]Krist, S. L., Thomas, J. I., Sellers, W. L., III, and Kjelgaard, S. O., "An Embedded Grid Formulation Applied to a Delta Wing," AIAA Paper 90-0429, 1990.

[24]Hummel, D., and Srinivasan, P. S., "Vortex Breakdown Effects on the Low-Speed Aerodynamic Characteristics of Slender Delta Wings in Symmetrical Flow," *Royal Aeronautical Society Journal*, Vol. 71, April 1967, pp. 319–322.

P. Givi
Associate Editor